A Conservative Cut-Cell Immersed Boundary Method for Accurate Simulation of Hypersonic Flows with Gas-Surface Interactions

Başkaya, A.O.; Hickel, S.

Publication date
2023

Published in
57th 3AF International Conference AERO2023 At: Bordeaux, France

Citation (APA)
Başkaya, A. O., & Hickel, S. (2023). A Conservative Cut-Cell Immersed Boundary Method for Accurate Simulation of Hypersonic Flows with Gas-Surface Interactions. In *57th 3AF International Conference AERO2023 At: Bordeaux, France*

Association Aéronautique et Astronautique de France

57th 3AF International Conference on Applied Aerodynamics
29 — 31 March 2023, Bordeaux – France

AERO2023-31-BASKAYA

A Conservative Cut-Cell Immersed Boundary Method for Accurate Simulation of Hypersonic Flows with Gas-Surface Interactions

Ata Onur Başkaya[(1)] and Stefan Hickel[(2)]

[(1)]*Aerodynamics Group, Faculty of Aerospace Engineering, TU Delft, The Netherlands, a.o.baskaya@tudelft.nl*

[(2)]*Aerodynamics Group, Faculty of Aerospace Engineering, TU Delft, The Netherlands, s.hickel@tudelft.nl*

ABSTRACT

A conservative cut-cell immersed boundary (IB) method including gas-surface interactions (GSI) for the simulation of atmospheric entry flows under thermochemical nonequilibrium (TCNE) conditions is presented. The performance of the method is demonstrated for three test cases: a compression ramp, a cylinder, and a plasma wind tunnel ablator sample. The computational predictions are in excellent agreement with reference simulations and experimental data for translational and vibrational temperature variations in the flow field, pressure and heat flux distributions over the geometries, and the mass blowing rates over a surface undergoing ablation.

1. INTRODUCTION

Atmospheric entry of capsules or space debris involve complex flow environments due to strong shock waves at hypersonic speeds, and high-temperature effects such as thermochemical nonequilibrium (TCNE) and interactions with the surface material. Depending on the characteristics of the surface material, these gas-surface interactions (GSI) result in catalysis as well as ablation. The latter process alleviates the heat load by means of physicochemical decomposition and mass loss, which alters the shape of the object as its surface recesses. Understanding these fluid-structure interactions is crucial for predicting the surface stresses and heat fluxes as well as the uncontrolled trajectory of space debris. Ground testing is indispensable for validation purposes; however, no facility can simultaneously replicate all aspects of atmospheric entry flows [13]. Hence, computational fluid dynamics (CFD) simulations are essential for the efficient aerothermodynamic analysis and design of future spacecraft.

Investigation of these regimes requires appropriate numerical schemes and computational grids for the accurate representation of strong shock waves and chemically reacting boundary layers. Most solvers used for these applications employ body-conforming structured grids [19, 20, 37]. In these solvers, accurate prediction of the flow field relies on careful alignment of the grid with the shock and the surface. In practice, this requirement demands strenuous effort from the user in generating high-quality body-conforming grids, especially for detailed features and incremental geometry updates [9]. Unstructured grids have also been explored; however, issues affecting the heat flux predictions at the surface were reported [10, 30]. A promising alternative is the use of adaptive mesh refinement (AMR) techniques based on piecewise Cartesian grids with immersed boundary (IB) methods, which offer a relatively straight-forward implementation of high-order schemes. There has been a recently growing interest in IB solvers for high-speed viscous compressible flows [1, 2, 7, 23, 32]. Especially for moving and deforming objects with complex shapes, IB methods are more robust and more efficient than body-conforming mesh-deformation methods.

This paper presents a conservative cut-cell IB method available in the INCA solver (https://www.inca-cfd.com) for the accurate simulation of hypersonic flows including the effects of GSI as encountered in atmospheric entry applications. Cut-cell IB methods are a straightforward extension of the finite-volume flux balance and thus satisfy mass, momentum and energy conservation exactly. Compared to standard cut-cell methods, the present method works on so-called cut elements, which provide sub-cell resolution of the geometry [25]. The verification and validation of the method is presented in a separate publication [4], which demonstrates the accurate modelling of the high-temperature physicochemical interactions and

the advantages of the present conservative IB methodology over nonconservative formulations.

In the present paper, the underlying numerical methodology is presented and demonstrated for three test cases: hypersonic flow over a compression ramp with perfect gas as well as with thermochemical nonequilibrium models, hypersonic flow in thermochemical nonequilibrium over a cylinder, and a graphite ablator exposed to nitrogen plasma. The governing equations and the thermochemical models are presented in Section 2. The cut-element IB methodology incorporating GSI is detailed in Section 3. Results of the case studies are discussed in Section 4, and concluding remarks are made in Section 5.

2. GOVERNING EQUATIONS

The compressible Navier-Stokes equations are solved in their conservative form for a reacting multicomponent fluid under thermochemical nonequilibrium including an additional transport equation for the vibrational energy [26],

$$\frac{\partial \rho_i}{\partial t} + \nabla \cdot (\rho_i \mathbf{u}) + \nabla \cdot \mathbf{J}_i = \dot{\omega}_i \,, \quad (1)$$

$$\frac{\partial \rho \mathbf{u}}{\partial t} + \nabla \cdot (\rho \mathbf{u} \otimes \mathbf{u}) + \nabla p - \nabla \cdot \boldsymbol{\tau} = 0 \,, \quad (2)$$

$$\frac{\partial \rho E}{\partial t} + \nabla \cdot [(\rho E + p)\,\mathbf{u}] + \nabla \cdot \mathbf{q} - \nabla \cdot (\boldsymbol{\tau} \cdot \mathbf{u}) = 0 \,, \quad (3)$$

$$\frac{\partial \rho e^{\mathrm{V}}}{\partial t} + \nabla \cdot \rho e^{\mathrm{V}} \mathbf{u} + \nabla \cdot \mathbf{q}^{\mathrm{V}} = \dot{\Omega} \,. \quad (4)$$

Here, ρ_i is the species partial density for the i^{th} species, $\mathbf{u}$ is the mixture average velocity, and $\dot{\omega}_i$ is the source term associated with the production or consumption of species due to chemical reactions. Moreover, ρ is the mixture density, p is the mixture pressure, and $E = e + u^2/2$ is the specific total energy, which is the sum of the thermodynamic internal energy e and the kinetic energy. The species diffusion flux $\mathbf{J}_i$, the viscous stress tensor $\boldsymbol{\tau}$, and the total heat flux $\mathbf{q}$ are detailed in the following paragraphs. External forces due to gravitational or magnetic effects, and radiative energy exchanges are not considered for the cases in this study.

For thermal nonequilibrium effects, Park's two-temperature model [26] is employed, which requires solving an energy equation for the vibrational thermal bath, denoted by the superscript V. The heat flux for the vibrational temperature is $\mathbf{q}^{\mathrm{V}}$, and the corresponding thermal conductivity

$$\lambda^{\mathrm{V}} = \sum_i \frac{\rho_i c_{p,i}^{\mathrm{V}}}{\sum_j x_j / \mathscr{D}_{ij}} \,, \quad (5)$$

is obtained by the Euken correction [16] with c_p^{V} as the vibrational specific heat at constant pressure, x_j as the mole fraction of the j^{th} species, and $\mathscr{D}_{ij}$ as the binary diffusion coefficients.

The energy exchange term $\dot{\Omega} = \dot{\Omega}^{\mathrm{TV}} + \dot{\Omega}^{\mathrm{CV}}$ in Eq. 4 describes how the system relaxes to equilibrium through energy exchanges between the vibrational mode and the translational mode, $\dot{\Omega}^{\mathrm{TV}}$, and chemical reactions, $\dot{\Omega}^{\mathrm{CV}}$. For the former, the Landau-Teller formulation is used as

$$\dot{\Omega}^{\mathrm{TV}} = \sum_m \dot{\Omega}_m^{\mathrm{TV}} = \sum_m \rho_m \frac{e_m^{\mathrm{V}}(T^{\mathrm{T}}) - e_m^{\mathrm{V}}(T^{\mathrm{V}})}{\tau_m^{\mathrm{TV}}} \quad (6)$$

where the summations are over each molecule m, and τ_m^{TV} is the relaxation time according to Park's correction [26] to the expression proposed by Millikan and White. A non-preferential dissociation model is used for the variation of the vibrational energy due to chemical reactions. This term is related to the chemical production rate of molecules $\dot{\omega}_m$ as

$$\dot{\Omega}^{\mathrm{CV}} = \sum_m \dot{\Omega}_m^{\mathrm{CV}} = \sum_m e_m^{\mathrm{V}} \dot{\omega}_m \,. \quad (7)$$

More intricate thermal nonequilibrium models are available [21], yet the current model has proven suitable for our range of applications [27].

The ideal gas assumption leads to the equation of state $p = \rho R T$, where $R = \mathscr{R}/\overline{M}$ is the mixture gas constant with the universal gas constant $\mathscr{R}$ and mixture average molar mass $\overline{M}$. These mixture properties are obtained according to Dalton's law through their constituent species as $p = \sum_i p_i$, $\rho = \sum_i \rho_i$, $R = \sum_i y_i R_i$, with the mass fractions $y_i = \rho_i / \rho$.

Fick's law is used for modeling diffusion with a correction to ensure conservation of mass

$$\mathbf{J}_i = -\rho D_{im} \nabla y_i + y_i \sum_j \rho D_{jm} \nabla y_j \,, \quad (8)$$

where

$$D_{im} = \frac{1 - x_i}{\sum_{j \neq i} x_j / \mathscr{D}_{ij}} \,, \quad (9)$$

are the mixture-averaged diffusion coefficients.

The viscous stress tensor is modeled assuming Stokes' hypothesis as

$$\boldsymbol{\tau} = \mu \left[\nabla \mathbf{u} + (\nabla \mathbf{u})^{\dagger} - \frac{2}{3} \nabla \cdot \mathbf{u} \boldsymbol{I} \right] \,, \quad (10)$$

where μ is the dynamic (shear) viscosity of the mixture.

The heat flux vector includes the contributions from conduction and mass diffusion,

$$\mathbf{q} = -\lambda \nabla T - \lambda^{\mathrm{V}} \nabla T^{\mathrm{V}} + \sum_i \mathbf{J}_i h_i(T, T^V) \,, \quad (11)$$

where T is the translational temperature and T^{V} is the vibrational temperature. The first two terms stem from Fourier's law and the last term refers to the diffusion of

enthalpy with h_i as the species partial enthalpy. Similarly, vibrational heat flux is written as

$$\mathbf{q}^{\mathrm{V}} = -\lambda^{\mathrm{V}} \nabla T^{\mathrm{V}} + \sum_i \mathbf{J}_i h_i^{\mathrm{V}}(T^{\mathrm{V}}) \,. \tag{12}$$

The flow solver INCA has been coupled with the MUlticomponent Thermodynamic And Transport properties for IONized gases in C++ (Mutation^{++}) library of the von Karman Institute, which provides accurate models for thermodynamic data, transport properties, chemical kinetics, and GSI. A detailed description of Mutation^{++} is presented by Scoggins et al. [31]. Most notably, species mass diffusivities, viscosities, and thermal conductivities are obtained from multicomponent Chapman-Enskog formulations [11] as opposed to the common approach of using simplified mixture rules [22, 29, 36]. Verification and validation of this coupling as well as further details on the models being used for the closure of the governing equations are presented by Başkaya et al. [4].

Catalytic and ablative surface boundary conditions are imposed by solving a mass balance [5, 31]

$$(\rho_i v_{blow})_{wall} + (J_i)_{wall} = \dot{\omega}_{i,wall} \,, \tag{13}$$

with v_{blow} as the surface-normal blowing velocity, which is nonzero only for an ablative boundary. Terms from left to right refer to convective flux due to blowing, diffusive flux, and a species source term due to surface reactions. A probability-based approach is employed for computing this chemical source term for the surface, written as

$$\dot{\omega}_{i,wall} = \gamma m_i \mathscr{F}_{i,impin} \,, \tag{14}$$

where $\gamma = \mathscr{F}_{i,react} / \mathscr{F}_{i,impin}$ is the ratio of reacting to impinging species fluxes and describes the efficiency of the process, and m_i is the mass of the i^{th} species [5]. Assuming the species at the wall have a Maxwellian distribution function, the impinging species flux is

$$\mathscr{F}_{i,impin} = n_i \sqrt{\frac{k_B T_w}{2\pi m_i}} \,, \tag{15}$$

where k_B is the Boltzmann constant, T_w is the wall temperature, and n_i is the number density of the i^{th} species [3]. The mass blowing rate $\dot{m} = \sum_i \dot{\omega}_{i,wall}$ determines the blowing velocity

$$v_{blow} = \frac{\dot{m}}{\sum_i \rho_i} \,. \tag{16}$$

Values obtained for species densities and mass blowing velocity are then imposed as boundary conditions for the Navier-Stokes equations.

3. NUMERICAL METHODS

The governing equations can be written as

$$\frac{\partial \mathbf{U}}{\partial t} + \nabla \cdot \mathbf{F}(\mathbf{U}) = \mathbf{S} \,, \tag{17}$$

where $\mathbf{U}$ is the vector of conserved variables, $\mathbf{F} = \mathbf{F}_{inv} + \mathbf{F}_{vis}$ is the sum of inviscid and viscous fluxes, and $\mathbf{S}$ is the vector of source terms. Along the x axis, they take the following forms:

$$\mathbf{U} = \begin{bmatrix} \rho_i \\ \rho u \\ \rho v \\ \rho w \\ \rho E \\ \rho e^{\mathrm{V}} \end{bmatrix}, \; \mathbf{F}_{inv} = \begin{bmatrix} \rho_i u \\ \rho u^2 + p \\ \rho uv \\ \rho uw \\ u(\rho E + p) \\ u \rho e^{\mathrm{V}} \end{bmatrix},$$

$$\mathbf{F}_{vis} = \begin{bmatrix} J_{\mathrm{x},i} \\ -\tau_{\mathrm{xx}} \\ -\tau_{\mathrm{xy}} \\ -\tau_{\mathrm{xz}} \\ -(\tau_{\mathrm{xx}} u + \tau_{\mathrm{xy}} v + \tau_{\mathrm{xz}} w) + q_{\mathrm{x}} \\ q_{\mathrm{x}}^{\mathrm{V}} \end{bmatrix}, \; \mathbf{S} = \begin{bmatrix} \dot{\omega}_i \\ 0 \\ 0 \\ 0 \\ 0 \\ \dot{\Omega} \end{bmatrix} .$$

INCA is a high-fidelity finite-volume solver for the compressible chemically reacting Navier-Stokes equations and provides a large number of different discretization schemes on three-dimensional block-Cartesian AMR grids [15, 24].

For the purposes of this study, a third-order weighted essentially non-oscillatory (WENO) scheme [18] with HLLC flux function [35] is selected to discretize the inviscid terms. WENO schemes provide high accuracy in smooth regions, while ensuring stable and sharp capturing of discontinuities. Second-order centered differences are used for the viscous terms and the explicit third-order Runge-Kutta scheme of Gottlieb and Shu [12] is selected for time integration.

Chemical source terms are treated using Strang's second-order time splitting scheme [34]. This leads to a system of ordinary differential equations (ODE) given as

$$\dot{y}_i = \frac{\dot{\omega}_i(\mathbf{y}, p, T, T^{\mathrm{V}})}{\rho} \,, \tag{18}$$

where $\dot{y}_i$ is the rate of change of mass fractions. This system is solved by the VODE library [8] using fifth-order backward differences.

3.1 Cut-Element IB Methodology

The employed cut-element based immersed boundary method is a consistent and conservative extension of the finite-volume flux balance that accounts for cells being split by boundaries [25, 28]. At the boundary that divides the fluid and the solid regions, fluxes are calculated according to cell-face apertures and interface exchange terms as illustrated in Fig. 1. For a given cell with the geometric indices $[i, j, k]$, the fluid and solid domains are separated by the interface $\Gamma_{i,j,k}$. The aperture $A_{i,j,k}$ denotes the fraction of the cell-face area that belongs to the

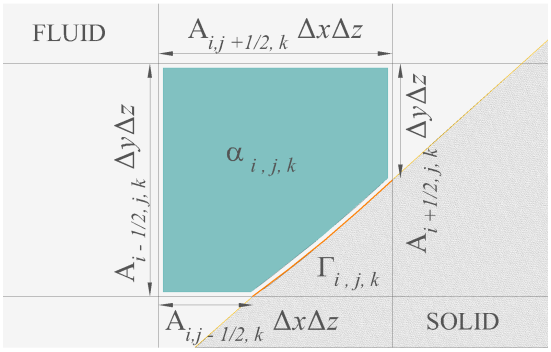

Figure 1: Sketch of a two-dimensional cut-cell in the immersed boundary method of INCA.

fluid domain. The fluid volume fraction of a cell is denoted by $\alpha_{i,j,k}$, such that the effective fluid volume of a cut cell is $(V_f)_{i,j,k} = \alpha_{i,j,k}\Delta x_i \Delta y_j \Delta z_k$.

Following the finite-volume methodology, integration of Eq. 17 over the fluid volume V_f for a time step $\Delta t = t^{n+1} - t^n$ yields

$$\int_{t^n}^{t^{n+1}} \left[\int_{V_f} \frac{\partial \mathbf{U}}{\partial t}\, dV + \int_{S_f} \mathbf{F}(\mathbf{U}) \cdot \mathbf{n}\, dS \right] dt = 0\,, \tag{19}$$

where S_f is the wetted surface of a given cell. Defining a volume average for the conserved variables of a cell as

$$\overline{\mathbf{U}}_{i,j,k} = \frac{1}{\alpha_{i,j,k}\Delta x_i \Delta y_j \Delta z_k} \int_{V_f} \mathbf{U} dV\,, \tag{20}$$

the three-dimensional discretization of Eq. 19 on a Cartesian grid is

$$\begin{aligned}
\alpha^{n+1}_{i,j,k}\overline{\mathbf{U}}^{n+1}_{i,j,k} = \alpha^{n}_{i,j,k}\overline{\mathbf{U}}^{n}_{i,j,k} \\
+ \frac{\Delta t}{\Delta x_i}\left[A_{i-1/2,j,k}\overline{\mathbf{F}}_{i-1/2,j,k} - A_{i+1/2,j,k}\overline{\mathbf{F}}_{i+1/2,j,k}\right] \\
+ \frac{\Delta t}{\Delta y_j}\left[A_{i,j-1/2,k}\overline{\mathbf{F}}_{i,j-1/2,k} - A_{i,j+1/2,k}\overline{\mathbf{F}}_{i,j+1/2,k}\right] \\
+ \frac{\Delta t}{\Delta z_k}\left[A_{i,j,k-1/2}\overline{\mathbf{F}}_{i,j,k-1/2} - A_{i,j,k+1/2}\overline{\mathbf{F}}_{i,j,k+1/2}\right] \\
+ \frac{\Delta t}{\Delta x_i \Delta y_j \Delta z_k}\mathbf{X}_{i,j,k}\,.
\end{aligned} \tag{21}$$

Note that $\overline{\mathbf{F}}$ refers to the face-averaged fluxes. Here, the discretization in time is presented for a forward Euler scheme, which corresponds to a sub-step of the employed Runge-Kutta scheme. The interface exchange term $\mathbf{X}_{i,j,k}$ represents the stresses and the fluxes through the fluid-solid interface. This term is essential for the GSI boundary condition as it will be discussed further on.

Instead of a single planar fluid-solid interface as in Fig. 1, the specific method in INCA accounts for multiple cut elements per cell [25, 28]. These cut-elements directly result from the intersection of the grid with the surface triangulation. The interface of each cut-cell is thus represented by several cut-elements belonging to different surface triangles. The exchange of mass (e.g. with surface reactions), momentum, and energy through these cut-elements is calculated from the prescribed boundary conditions and interpolated fluid values at a point within the fluid domain, which is generally a half cell length away from the interface. The value of a variable at this fluid point is acquired by interpolation from the surrounding cell values and the boundary conditions. In addition, a layer of ghost cells within the solid body is employed to allow for the use of unmodified stencils throughout the domain.

The interface exchange term $\mathbf{X}_{i,j,k}$ is expressed as a sum of the contributions of all cut elements

$$\mathbf{X}_{i,j,k} = \sum_{el} \mathbf{X}_{el}\,, \tag{22}$$

where the index el denotes cut elements for a given cell, and

$$\mathbf{X}_{el} = \mathbf{X}^p_{el} + \mathbf{X}^v_{el} + \mathbf{X}^q_{el} + \mathbf{X}^m_{el}\,, \tag{23}$$

where, from left to right, the terms refer to pressure, viscous stresses, heat transfer, and mass exchange. The last term incorporates GSI in addition to the original formulation described by Örley et al. [25] and Pasquariello et al. [28]. We assume that thermal equilibrium is reached at the surface, therefore there is no interface exchange for the vibrational energy.

The pressure term is given by

$$\mathbf{X}^p_{el} = \begin{bmatrix} 0 \\ \Delta\Gamma_{el}\, p_{\Gamma,el}\, n^{\Gamma,el}_{\mathrm{x}} \\ \Delta\Gamma_{el}\, p_{\Gamma,el}\, n^{\Gamma,el}_{\mathrm{y}} \\ \Delta\Gamma_{el}\, p_{\Gamma,el}\, n^{\Gamma,el}_{\mathrm{z}} \\ \Delta\Gamma_{el}\, p_{\Gamma,el}\left(\mathbf{v}^{\Gamma,el}\cdot\mathbf{n}^{\Gamma,el}\right) \\ 0 \end{bmatrix}, \tag{24}$$

where $p_{\Gamma,el}$ is the element interface pressure obtained by solving a one-sided face-normal Riemann problem, $\Delta\Gamma_{el}$ is the interface area of the cut element, $n^{\Gamma,el}$ refers to the normal vector of the element, and $\mathbf{v}^{\Gamma,el}$ is the interface velocity evaluated at the surface centroid. Similarly, the viscous stresses are

$$\mathbf{X}^v_{el} = \begin{bmatrix} 0 \\ \Delta\Gamma_{el}\left(\boldsymbol{\tau}\cdot\mathbf{n}^{\Gamma,el}\right)_{\mathrm{x}} \\ \Delta\Gamma_{el}\left(\boldsymbol{\tau}\cdot\mathbf{n}^{\Gamma,el}\right)_{\mathrm{y}} \\ \Delta\Gamma_{el}\left(\boldsymbol{\tau}\cdot\mathbf{n}^{\Gamma,el}\right)_{\mathrm{z}} \\ \Delta\Gamma_{el}\left(\boldsymbol{\tau}\cdot\mathbf{v}^{\Gamma,el}\right)\cdot\mathbf{n}^{\Gamma,el} \\ 0 \end{bmatrix}, \tag{25}$$

where $\boldsymbol{\tau}$ is the local stress tensor. The velocity gradient in the local stress tensor is approximated by the difference

between the interpolation point velocity and the interface velocity. The heat exchange is given by

$$\mathbf{X}_{el}^{q} = \begin{bmatrix} 0 \\ 0 \\ 0 \\ 0 \\ \Delta\Gamma_{el} \left(\mathbf{q}^{\Gamma,el} \cdot \mathbf{n}^{\Gamma,el} \right) \\ 0 \end{bmatrix}. \tag{26}$$

For a reacting surface, exchange of mass with the solid is modeled as

$$\mathbf{X}_{el}^{m} = \begin{bmatrix} \Delta\Gamma_{el}\, \dot{\omega}_{i,wall} \\ \Delta\Gamma_{el}\, \dot{m} \left(\mathbf{v}_{blow}^{\Gamma,el} \cdot \mathbf{n}^{\Gamma,el} \right)_{\mathrm{x}} \\ \Delta\Gamma_{el}\, \dot{m} \left(\mathbf{v}_{blow}^{\Gamma,el} \cdot \mathbf{n}^{\Gamma,el} \right)_{\mathrm{y}} \\ \Delta\Gamma_{el}\, \dot{m} \left(\mathbf{v}_{blow}^{\Gamma,el} \cdot \mathbf{n}^{\Gamma,el} \right)_{\mathrm{z}} \\ \Delta\Gamma_{el}\, \dot{m} \left(h^{\Gamma,el} + \frac{1}{2} \| \mathbf{v}_{blow}^{\Gamma,el} \|^2 \right) \\ 0 \end{bmatrix}, \tag{27}$$

where $\dot{m}$ is the total mass blowing rate, $\mathbf{v}_{blow}^{\Gamma,el}$ is the blowing velocity given by Eq. 16, and $h^{\Gamma,el}$ is the enthalpy of the produced species. Naturally, the sum of the species mass exchange terms yields the global mass exchange $\Delta\Gamma_{el}\,\dot{m}$ and it is only non-zero if the surface is ablative. However, as long as the surface is reacting, catalytic reactions will alter the surface species compositions and therefore lead to non-zero species mass exchange.

4. RESULTS

4.1 Compression Ramp

The first test case is a Mach 11.63 compression ramp flow based on the experimental campaigns of Holden [17]. The numerical setup follows Brahmachary et al. [6] and McQuaid et al. [23] who modeled air as a perfect gas. In addition to this perfect gas case, we also present simulations with thermochemical nonequilibrium. The geometry consist of a straight section of 0.4394 m and a 15° ramp beyond this point. The total length of the computational domain is 0.7 m. Freestream conditions are given in Table 1.

Table 1: Case specifications for the compression ramp.

u_∞ [m/s]	T_∞ [K]	T_{wall} [K]	p_∞ [Pa]
1908.9	67.05	294.38	25

Grid resolutions near the wall are 5×10^{-5} m for the present simulations with INCA, 2×10^{-5} m for Brahmachary et al., and 3×10^{-5} m for McQuaid et al.

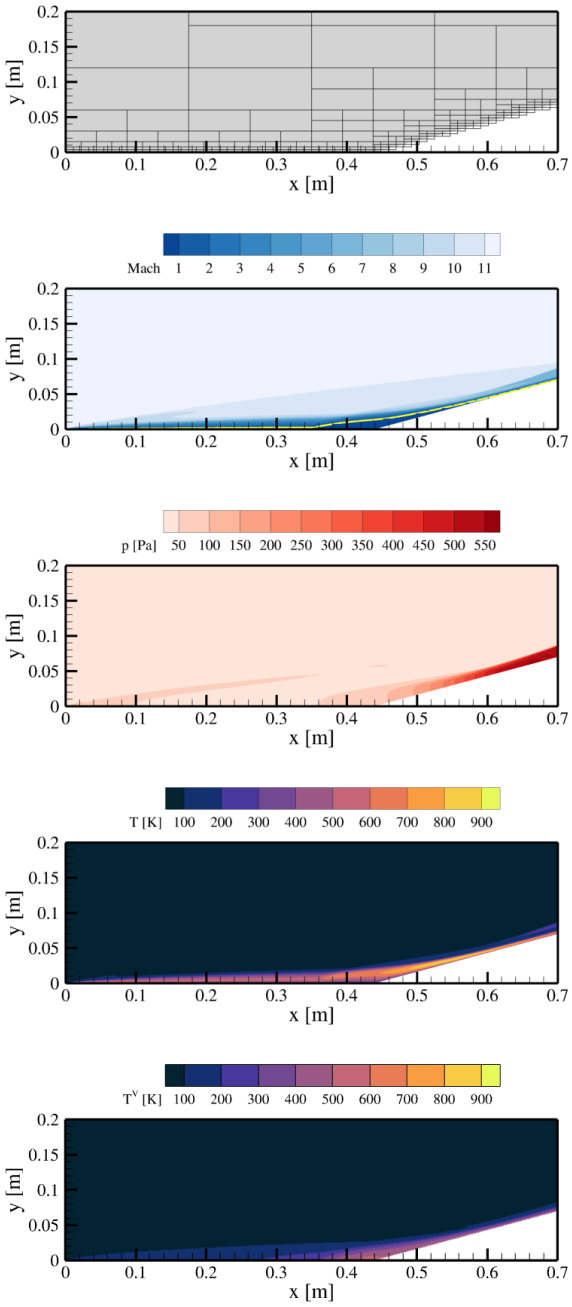

Figure 2: Block structure of the computational mesh and flow fields showing Mach number (sonic line indicated as the bright line), pressure, translational temperature, and vibrational temperature contours for the compression ramp case with thermochemical nonequilibrium.

The flow field is visualized in Fig. 2, where the separating shock wave is impinging on the ramp. The results

for the pressure coefficient

$$C_p = \frac{p_{wall} - p_\infty}{0.5\rho_\infty u_\infty^2}, \tag{28}$$

and Stanton number

$$St = \frac{q_{wall}}{\rho_\infty U_\infty c_p (T_r - T_{wall})}, \tag{29}$$

distributions along the surface are presented in Fig. 3. Results for the perfect gas and thermochemical nonequilibrium (TCNE) models are compared. The results obtained with our perfect gas model are in excellent agreement with the numerical results of McQuaid et al. [23]. Due to the low temperature at the freestream, only a weak vibrational excitation is observed. Nevertheless, the shock is moved considerably closer to the ramp in the TCNE results and yield pressure coefficients marginally closer to the experimental results.

For Stanton numbers, corresponding to the different definitions used by the authors of the reference results, two sets of results are shown. Firstly, by taking $T_r = T_{total}$ in accordance with Brahmachary et al. [6], and secondly, by taking T_r based on a recovery factor of 0.89 in line with McQuaid et al. [23]. Both definitions used for the Stanton number agree well with their corresponding reference results with the perfect gas assumption. Stanton numbers match the experimental reference results very well and almost exactly with the TCNE model.

4.2 Cylinder

A 5-species air flow at a Mach number of 12.7 over a cylinder of 0.1 m radius is considered to study the method under thermochemical nonequilibrium conditions. Sekhar et al. [33], provide reference results obtained with the well-established DPLR solver. Freestream conditions are presented in Table 2. The 5-species air mixture consists of $[N_2, O_2, NO, N, O]$. A rather coarse grid is used with 7×10^{-4} m resolution at the surface, where an adiabatic boundary condition is imposed.

Table 2: Case specifications for the cylinder.

u_∞ [m/s]	T_∞ [K]	p_∞ [Pa]	$y(N_2)$	$y(O_2)$
3570	195.96	90	0.7671	0.2329

The results for the translational and vibrational temperature contours, and their distributions along the stagnation line are presented in Fig. 4 and in Fig. 5. The present results are shown as colored contours overlaid with bright contour lines for the reference data. Predictions with the present method match almost exactly with the reference results. The thermal nonequilibrium beyond the shock and the relaxation to thermal equilibrium downstream are very well captured. Slight differences are expected to be due to a coarser grid resolution near the shock for the reference simulations.

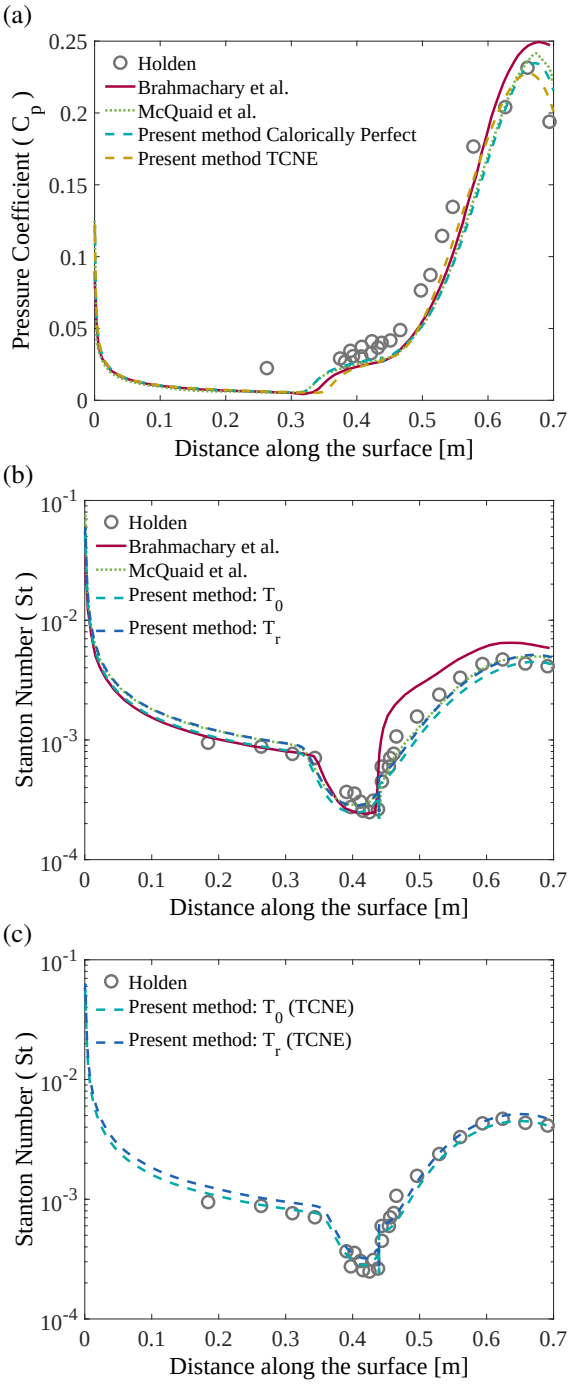

Figure 3: Comparison of (a) pressure coefficients, (b) Stanton numbers along the surface with the perfect gas models, and (c) Stanton numbers along the surface with the TCNE model for the compression ramp case.

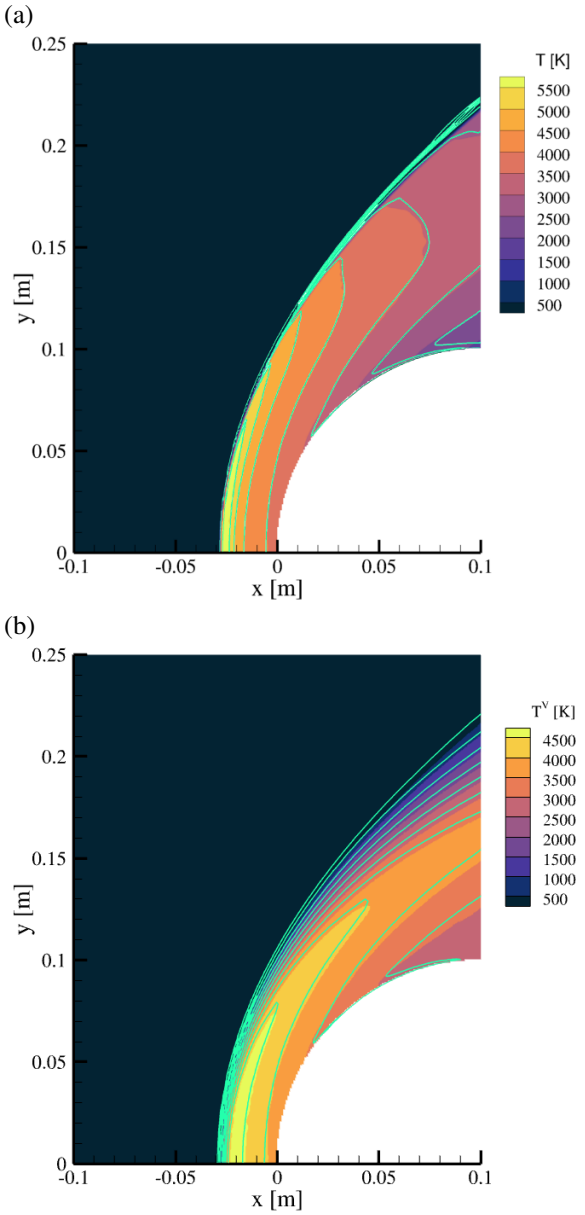

Figure 4: Comparison of (a) translational and (b) vibrational temperature contours for the cylinder case. Reference data by DPLR [33] is overlaid as bright lines.

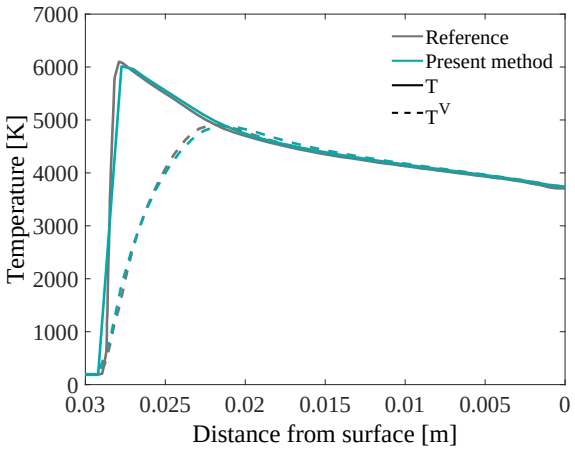

Figure 5: Variation of translational and vibrational temperatures along the stagnation line for the cylinder case. Reference data is provided by DPLR [33].

4.3 Graphite Ablator

A subsonic plasma wind tunnel experiment conducted by Helber et al. [14] at the von Karman Institute is simulated to demonstrate the ablative boundary condition. The experiment exposes a graphite sample with a hemispherical nose of radius 25 mm to nitrogen plasma. The sample undergoes ablation through nitridation reactions

$$\mathrm{C}_{(\mathrm{solid})} + \mathrm{N} \rightarrow \mathrm{CN}\,, \tag{30}$$

with the reaction probability

$$\gamma = 7.91 \cdot 10^{-2} \exp\left(-\frac{5663}{T_{\mathrm{wall}}}\right). \tag{31}$$

The nitridation efficiency was calibrated based on these particular experiments [14]. The experimental test case was simplified by Başkaya et al. [4] to a 2-D geometry without ionized species to reduce the computational cost. Freestream conditions for this case are given in Table 3. A 6-species mixture of $[\mathrm{N_2}, \mathrm{N}, \mathrm{CN}, \mathrm{C_3}, \mathrm{C_2}, \mathrm{C}]$ is considered. Reference data for this case is obtained with the US3D solver employing body-conforming meshes. US3D is an extensively validated high-fidelity solver, which uses the same models for thermochemistry and GSI as INCA in this study [4].

Table 3: Case specifications for the graphite ablator.

u_∞ [m/s]	T_∞ [K]	T_{wall} [K]	p_∞ [Pa]	$y(\mathrm{N_2})$
1570	10280	2407	1500	9.777e-05

The mass fractions along the stagnation line and the mass blowing rates over the wall are shown in Fig. 6. The predictions of the present method agree remarkably well with the results of the reference solver. Coarse results with our method correspond to a grid resolution of 1×10^{-5} m at the wall, in line with the reference. An additional simulation with a finer grid with 5×10^{-6} m cell size at the wall is also performed to ensure the solution is grid converged.

5. CONCLUSION

A fully conservative cut-element immersed-boundary method for hypersonic flows under the influence of ther-

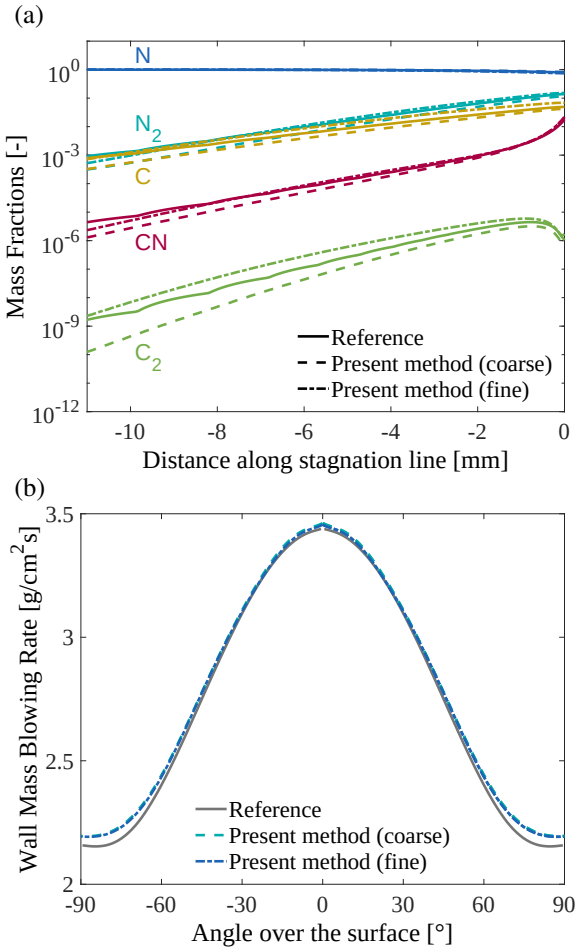

Figure 6: Comparison of (a) mass fractions along the stagnation line and (b) mass blowing rates over the surface for the graphite ablator case. Reference data is provided by the US3D solver [4].

mochemical nonequilibrium and gas-surface interactions has been presented and demonstrated for hypersonic flow over a compression ramp, hypersonic flow over a cylinder, and a graphite ablator exposed to nitrogen plasma. All of the results have shown good agreement with the references, indicating that the method is highly suitable for atmospheric entry applications. Future studies will explore more challenging scenarios that exploit the full potential of an adaptive mesh refinement immersed-boundary method for ablative recession and shape change.

REFERENCES

[1] R. Arslanbekov, V. Kolobov, and A. Frolova. Analysis of compressible viscous flow solvers with adaptive cartesian mesh. *AIAA paper 2011-3381*, 2011.

[2] C. Atkins and R. Deiterding. Towards a strand-Cartesian solver for modelling hypersonic flows in thermochemical non-equilibrium. *AIAA paper 2020-2404*, 2020.

[3] P. F. Barbante. *Accurate and efficient modelling of high temperature nonequilibrium air flows*. PhD thesis, Université libre de Bruxelles, 2001.

[4] A. O. Başkaya, M. Capriati, D. Ninni, F. Bonelli, G. Pascazio, A. Turchi, T. Magin, and S. Hickel. Verification and validation of immersed boundary solvers for hypersonic flows with gas-surface interactions. *AIAA paper 2022-3276*, 2022.

[5] G. Bellas Chatzigeorgis, A. Turchi, A. Viladegut, O. Chazot, P. F. Barbante, and T. Magin. Development of catalytic and ablative gas-surface interaction models for the simulation of reacting gas mixtures. *AIAA paper 2017-4499*, 2017.

[6] S. Brahmachary, G. Natarajan, V. Kulkarni, and N. Sahoo. A sharp-interface immersed boundary method for high-speed compressible flows. In *Immersed Boundary Method*, pages 251–275. Springer, 2020.

[7] S. Brahmachary, G. Natarajan, V. Kulkarni, N. Sahoo, V. Ashok, and V. Kumar. Role of solution reconstruction in hypersonic viscous computations using a sharp interface immersed boundary method. *Physical Review E*, 103(4):043302, 2021.

[8] P. N. Brown, G. D. Byrne, and A. C. Hindmarsh. VODE: A variable-coefficient ODE solver. *SIAM Journal on Scientific and Statistical Computing*, 10(5):1038–1051, 1989.

[9] G. Candler, D. Mavriplis, and L. Trevino. Current status and future prospects for the numerical simulation of hypersonic flows. *AIAA paper 2009-153*, 2009.

[10] G. V. Candler, H. B. Johnson, I. Nompelis, V. M. Gidzak, P. K. Subbareddy, and M. Barnhardt. Development of the US3D code for advanced compressible and reacting flow simulations. *AIAA paper 2015-1893*, 2015.

[11] S. Chapman and T. G. Cowling. *The mathematical theory of non-uniform gases: an account of the kinetic theory of viscosity, thermal conduction and diffusion in gases*. Cambridge University Press, 1990.

[12] S. Gottlieb and C.-W. Shu. Total variation diminishing Runge-Kutta schemes. *Mathematics of computation*, 67(221):73–85, 1998.

[13] S. Gu and H. Olivier. Capabilities and limitations of existing hypersonic facilities. *Progress in Aerospace Sciences*, 113:100607, 2020.

[14] B. Helber, A. Turchi, and T. E. Magin. Determination of active nitridation reaction efficiency of graphite in inductively coupled plasma flows. *Carbon*, 125:582–594, 2017.

[15] S. Hickel, C. P. Egerer, and J. Larsson. Subgrid-scale modeling for implicit large eddy simulation of compressible flows and shock-turbulence interaction. *Physics of Fluids*, 26(10):106101, 2014.

[16] J. O. Hirschfelder, C. F. Curtiss, R. B. Bird, and M. G. Mayer. *Molecular theory of gases and liquids*, volume 165. Wiley New York, 1964.

[17] M. Holden. A study of flow separation in regions of shock wave-boundary layer interaction in hypersonic flow. *AIAA paper 1978-1169*, 1978.

[18] G.-S. Jiang and C.-W. Shu. Efficient implementation of weighted eno schemes. *Journal of Computational Physics*, 126(1):202–228, 1996.

[19] D. Knight, O. Chazot, J. Austin, M. A. Badr, G. Candler, B. Celik, D. de Rosa, R. Donelli, J. Komives, A. Lani, et al. Assessment of predictive capabilities for aerodynamic heating in hypersonic flow. *Progress in Aerospace Sciences*, 90:39–53, 2017.

[20] D. Knight, J. Longo, D. Drikakis, D. Gaitonde, A. Lani, I. Nompelis, B. Reimann, and L. Walpot. Assessment of CFD capability for prediction of hypersonic shock interactions. *Progress in Aerospace Sciences*, 48:8–26, 2012.

[21] T. E. Magin, M. Panesi, A. Bourdon, R. L. Jaffe, and D. W. Schwenke. Coarse-grain model for internal energy excitation and dissociation of molecular nitrogen. *Chemical Physics*, 398:90–95, 2012.

[22] E. Mason and S. Saxena. Approximate formula for the thermal conductivity of gas mixtures. *The Physics of Fluids*, 1(5):361–369, 1958.

[23] J. A. McQuaid, A. L. Zibitsker, B. Saikia, A. Martin, and C. Brehm. An immersed boundary method for hypersonic viscous flows. *AIAA paper 2021-0926*, 2021.

[24] H. Müller, C. A. Niedermeier, J. Matheis, M. Pfitzner, and S. Hickel. Large-eddy simulation of nitrogen injection at trans-and supercritical conditions. *Physics of Fluids*, 28(1):015102, 2016.

[25] F. Örley, V. Pasquariello, S. Hickel, and N. A. Adams. Cut-element based immersed boundary method for moving geometries in compressible liquid flows with cavitation. *Journal of Computational Physics*, 283:1–22, 2015.

[26] C. Park. *Nonequilibrium hypersonic aerothermodynamics*. 1989.

[27] C. Park. The limits of two-temperature kinetic model in air. *AIAA paper 2010-911*, 2010.

[28] V. Pasquariello, G. Hammerl, F. Örley, S. Hickel, C. Danowski, A. Popp, W. A. Wall, and N. A. Adams. A cut-cell finite volume–finite element coupling approach for fluid–structure interaction in compressible flow. *Journal of Computational Physics*, 307:670–695, 2016.

[29] G. Sarma. Physico–chemical modelling in hypersonic flow simulation. *Progress in Aerospace Sciences*, 36(3-4):281–349, 2000.

[30] L. Scalabrin and I. Boyd. Development of an unstructured navier-stokes solver for hypersonic nonequilibrium aerothermodynamics. *AIAA paper 2005-5203*, 2005.

[31] J. B. Scoggins, V. Leroy, G. Bellas-Chatzigeorgis, B. Dias, and T. E. Magin. Mutation++: Multicomponent thermodynamic and transport properties for ionized gases in c++. *SoftwareX*, 12:100575, 2020.

[32] S. K. Sekhar and S. M. Ruffin. Predictions of convective heat transfer rates using a Cartesian grid solver for hypersonic flows. *AIAA paper 2013-2645*, 2013.

[33] S. K. Sekhar, M. Zaki, S. Ruffin, V. Kolobov, and R. Arslanbekov. Evaluation of viscous flow solvers with adaptive cartesian meshes for hypersonic flows. *AIAA paper 2011-4035*, 2011.

[34] G. Strang. On the construction and comparison of difference schemes. *SIAM Journal on Numerical Analysis*, 5(3):506–517, 1968.

[35] E. F. Toro. *Riemann solvers and numerical methods for fluid dynamics: a practical introduction*. Springer Science & Business Media, 2013.

[36] C. Wilke. A viscosity equation for gas mixtures. *The Journal of Chemical Physics*, 18(4):517–519, 1950.

[37] M. J. Wright, T. White, and N. Mangini. *Data Parallel Line Relaxation (DPLR) Code User Manual: Acadia Version 4.01. 1*. National Aeronautics and Space Administration, Ames Research Center, 2009.